J. Fluid Mech. (2007), *vol.* 590, *pp.* 209–237. © 2007 Cambridge University Press
doi:10.1017/S0022112007007987 Printed in the United Kingdom

Proximal bodies in hypersonic flow

STUART J. LAURENCE[1], R. DEITERDING[2] AND H. G. HORNUNG[1]

[1]Graduate Aeronautical Laboratories, California Institute of Technology, Pasadena, CA 91125, USA

[2]Oak Ridge National Laboratory, PO Box 2008 MS6367, Oak Ridge, TN 37831, USA

(Received 9 February 2007 and in revised form 13 June 2007)

Hypersonic flows involving two or more bodies travelling in close proximity to one another are encountered in several important situations. The present work seeks to explore one aspect of the resulting flow problem by investigating the forces experienced by a secondary body when it is within the domain of influence of a primary body travelling at hypersonic speeds.

An analytical methodology based on the blast wave analogy is developed and used to predict the secondary force coefficients for simple geometries in both two and three dimensions. When the secondary body is entirely inside the primary shocked region, the nature of the lateral force coefficient is found to depend strongly on the relative size of the two bodies. For two spheres, the methodology predicts that the secondary body will experience an exclusively attractive lateral force if the secondary diameter is larger than one-sixth of the primary diameter. The analytical results are compared with those from numerical simulations and reasonable agreement is observed if an appropriate normalization for the relative lateral displacement of the two bodies is used.

Results from a series of experiments in the T5 hypervelocity shock tunnel are also presented and compared with perfect-gas numerical simulations, with good agreement. A new force-measurement technique for short-duration hypersonic facilities, enabling the experimental simulation of the proximal bodies problem, is described. This technique provides two independent means of measurement, and the agreement observed between the two gives a further degree of confidence in the results obtained.

1. Introduction

Aerodynamic interactions between two or more bodies travelling at hypersonic speeds may occur in several important situations, both natural and man-made. We may point to launch vehicle stage separation, re-entry of either multiple vehicles or a single vehicle with a trailing ballute, and hypersonic store separation as man-made instances, whereas the planetary entry of a binary asteroid system and atmospheric meteoroid fragmentation represent naturally occurring examples in which such interactions may be encountered.

Previously, several authors have investigated problems involving aerodynamic interactions between hypersonic proximal bodies in association with modelling the behaviour of a fragmented meteoroid in a planetary atmosphere. Among the first to explore such a problem were Passey & Melosh (1980), who looked at possible mechanisms for cross-range dispersion of fragments in crater fields. They concluded that the combined effects of bow shock interactions, crushing deceleration, and

https://doi.org/10.1017/S0022112007007987 Published online by Cambridge University Press

possibly spinning of the parent meteoroid were primarily responsible. They also obtained an estimate for the transverse velocity of two fragments resulting from near-field shock interactions. Artem'eva & Shuvalov (1996) carried out numerical simulations of two fragments travelling in various relative configurations and found that when a secondary fragment was travelling within the shocked region created by a primary fragment, it experienced a force towards the axis of travel of the primary. In further simulations (Artemieva & Shuvalov 2001), these authors found that this phenomenon resulted in a collimation effect for a large number of fragments. This effect had previously been noted in experiments using the NASA–Ames vertical gun by Schultz & Sugita (1994).

Extensive experimental studies relevant to the current problem have also been carried out in the context of store and stage separation at hypersonic speeds. Particularly noteworthy are the captive trajectory systems developed at the Arnold Engineering and Development Center for store separation testing (Carman 1980) and more recently applied to the problem of risk reduction during stage separation of the NASA Hyper-X vehicle (Woods, Holland & DiFulvio 2001).

The current work is concerned with investigating a relatively simple version of the hypersonic proximal bodies problem, namely with determining the forces acting on a secondary body when it is travelling at some point within the shocked region created by a hypersonic primary body. We hereinafter refer to these two bodies simply as the secondary and the primary. Within this simplified problem, we identify three main physical regions in which we would expect the nature of the secondary forces to differ qualitatively. First, if the secondary is travelling in the wake region immediately behind the primary, the forces experienced will be small because of aerodynamic shielding. If the secondary lateral displacement is subsequently increased such that it is exposed to the primary-shock-processed flow, we would expect the axial (drag) force to be increased over the prior situation, but it is not immediately obvious whether the lateral force will be attractive or repulsive (relative to the primary axis of travel). Finally, if the lateral displacement of the secondary is increased further, so that it is impinged upon by the primary bow shock, the shock interactions will produce locally high pressure on the front of the secondary, resulting in a large drag force. Also, as the flow on the outer side of the secondary will be effectively singly shocked, while that on the inner side will be doubly shocked and thus at a higher pressure, we would expect a repulsive lateral force to develop in this configuration.

In § 3, an analytical model is developed that is valid in the second region described above. Numerical simulations covering all three regions are outlined in § 4, and results from these are compared with analytical results in § 5. In § 6, we describe a series of experimental simulations of configurations falling in the latter two regions. To enable this experimental investigation, a new force-measurement technique for hypervelocity facilities has been developed; a review of force-measurement techniques for shock-driven hypersonic facilities is presented in § 2. Conclusions are drawn in § 7.

In order to gain a general understanding of the proximal bodies problem, the study will be concerned with relatively simple geometries: we will limit ourselves to the cases of two circular cylinders and two spheres. In either case, the two bodies will be assumed to be stationary with respect to one another.

2. Review of force-measurement techniques in hypervelocity facilities

As part of the current study, experimental force measurements have been carried out in the T5 hypervelocity shock tunnel at the California Institute of Technology.

https://doi.org/10.1017/S0022112007007987 Published online by Cambridge University Press

Force- and moment-measurement in high-enthalpy hypersonic wind tunnels, such as T5, has traditionally been restricted by the short test time intrinsic to these facilities. This flow time can be less than the period of the lowest natural frequency of a typical model and support, rendering measurement by conventional force balance techniques impractical. This has necessitated the development of other techniques. These may be loosely divided into two groups.

The first group consists of attempts to modify traditional force balance techniques so that they are more suited to short duration measurements. Storkmann, Olivier & Gronig (1998) combined a model of high natural frequency (above 1 kHz) with accelerometers mounted in either the model or support to compensate for support oscillations. Measurements were made using a six-component strain gauge balance at two facilities: the Aachen shock tunnel TH2 and the Longshot facility at the von Kármán Institute in Brussels. The success of this method appears to be highly dependent on model geometry, however. Results for a cone model showed good agreement with reference data, but agreement for a capsule model was less satisfactory, and the technique could not be applied to slender bodies, as such geometries are unable to accommodate internal mounting of the balance.

Another technique along these lines is the stress-wave force balance technique, first proposed by Sanderson & Simmons (1991). This technique was developed for use with long models for which the test time is just sufficient to establish steady flow over the model, but not sufficent to establish stress equilibrium within the model. Thus, instead of measuring steady-state forces, this technique involves the interpretation of stress waves induced within the model, necessitating extensive calibration to determine the response function of the system. Mee (2003) achieved 3 % accuracy in calibration studies for this technique and performed measurements in the T4 shock tunnel at the University of Queensland, Australia. These, however, were limited to a single component drag measurement – accuracy in earlier attempts at multi-component force measurement (Mee, Daniel & Simmons 1996) was limited to 11 % accuracy. An attempt was made to apply this method to three-component force measurements on a large scramjet model (Robinson *et al.* 2004), but in this configuration the measurements were adversely affected by facility vibrations.

The second group consists of techniques that make use of a support allowing for free-floating model behaviour during the test time. The short test time of the relevant facilities is actually an advantage for such techniques, as even for high loads the extent of motion of the model during the test time will be extremely small. Sahoo *et al.* (2003) implemented a method in which the model was mounted in flexible rubber bushes, allowing free-floating behaviour in flows of millisecond duration. The force and moments were measured during this period by means of embedded accelerometers. These authors achieved good agreement with theoretical values (typically 3–8 %) in a series of measurements on blunted cones in the HST2 hypersonic shock tunnel at the Indian Institute of Science, Bangalore. This is a relatively low-load facility, however – dynamic pressures in a facility such as the T5 are typically higher by an order of magnitude or more. It is thus questionable whether model motions in these facilities could be accommodated by such a set-up. This technique also has the disadvantage of requiring extensive finite-element modelling, and the required mounting limits the geometries that may be simulated. Joarder & Jagadeesh (2004) implemented another free-floating technique in the HST2 facility, but this was limited to drag measurements.

Naumann *et al.* (1993) devised a method to allow for free flight during the steady-flow period whereby the model was mounted on a support that released just prior

https://doi.org/10.1017/S0022112007007987 Published online by Cambridge University Press

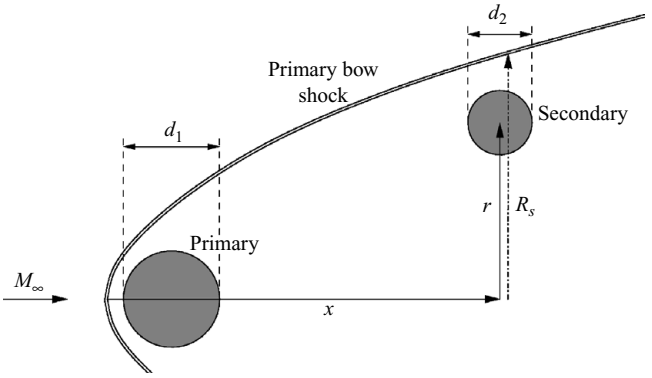


FIGURE 1. Representative physical situation for which the analytical model is developed. The two bodies may be either circular cylinders or spheres.

to the onset of the flow and tightened again shortly afterwards. Again, forces and moments were measured by means of accelerometers embedded in the model. This method relied on a cumbersome model support, however, which again limited the geometries that could be studied. Tanno *et al.* (2004) measured the forces generated by the interaction of a shock wave with a sphere in the vertical shock tube at the Interdisciplinary Shock Wave Research Center at Tohoku University. The sphere was suspended from a wire of sufficient length ($\sim$4 m) that tensile stress waves in the wire had a negligible effect during the test time. Obviously, such a suspension method is not practical in a typical horizontal flow wind tunnel.

The technique that has been developed in the present work falls in this latter group. A simple support system consisting of cotton thread, that is destroyed at the onset of the flow, is used in conjunction with a catcher that terminates the model motion after the end of the test time. Accelerations are recorded by an embedded accelerometer and by images taken with a high-speed digital camera. We are grateful to one of the referees for bringing to our attention that a similar suspension and force-measurement technique had been employed by Warren, Kaegi & Geiger (1961).

3. Analytical modelling

First, we formulate an analytical model to predict the forces acting on the secondary for configurations in which it lies entirely within the primary shocked region. For simplicity, a uniform free stream consisting of a perfect gas will be assumed.

The situation under consideration is shown in figure 1 and the problem parameters are indicated. The two bodies may be either both circular cylinders or spheres. The primary, of diameter d_1, generates a bow shock of radius $R_s(x)$, where x is the axial displacement measured from the leading point of the shock. The secondary, of diameter $d_2 < d_1$, is located downstream of the primary shock at a lateral displacement r. We wish to determine the axial (drag) and lateral (lift) force components on the secondary.

In hypersonic blunt-body flows, the viscous force contributions may often be neglected in favour of the pressure contributions, and thus, to approximate these force components, we require an estimate of the pressure distribution on the surface of the secondary. The assumption of a large Mach number allows us to make use of two results from classical hypersonics that are critical to our model. First, the blast wave analogy is used to approximate the flow conditions within the shocked region

https://doi.org/10.1017/S0022112007007987 Published online by Cambridge University Press

created by the primary, and secondly, given knowledge of these conditions, a modified version of the Newtonian distribution is used to approximate the secondary surface pressure distribution.

The blast wave analogy relates the flow produced by a body moving at hypersonic speeds to that produced by a point explosion. A similarity solution to the latter problem in a uniform, perfect gas atmosphere was first proposed by Taylor (1950) and full analytic solutions were subsequently obtained by Sedov (1959) in one, two and three space dimensions. The analogous flow produced by a hypersonic body (with appropriate symmetry) may be obtained by use of the equivalence principle, in which the time variable in the point explosion solution (of one dimension less than that of the body) is replaced by x/V, where V is the speed of the body in the (negative) x-direction. The shock radius obtained scales as $R_s \propto x^{2/3}$ for a two-dimensional (symmetric) body and $R_s \propto x^{1/2}$ for a three-dimensional (axisymmetric) body. The constant of proportionality in each case depends on the drag coefficient and the projected frontal surface area of the body, and the ratio of specific heats of the gas.

The blast wave analogy is most appropriate for approximating the flow produced by a rod- or plate-like blunt-nosed body, rather than the compact bodies we are interested in here. It is thus to be understood that our results are not valid in the wake region immediately behind the body and also that physical features such as separation shocks are absent from our model. The blast wave solution is also known to have a number of intrinsic problems, even when used for more appropriate geometries. A salient discussion of these may be found, for example, in Hayes & Probstein (1966). For our purposes, the most important of these problems is the presence of an entropy wake in the solution that is significantly stronger than that in the corresponding physical flow. This leads to questionable results for lateral secondary displacements extending out past the influence of the body wake region. A final problem with the blast wave solution is that it is known to produce a somewhat smaller shock radius than that produced by a physical blunt body (see, for example, Lukasiewicz 1962). A further discussion of this last problem appears in § 5.3.

3.1. *Two-dimensional modelling*

We first consider the two-dimensional case in which both bodies are circular cylinders and develop an approximation to the forces, per unit depth, on the secondary. The flow solution in the primary shocked region is assumed to be given by the two-dimensional (planar) blast wave analogy, but to approximate the pressure distribution on the secondary, let us first consider the same body travelling in the uniform hypersonic free stream outside the shocked region, the conditions of which we denote by the subscript ∞. For large Mach numbers, a good approximation to the pressure distribution is the modified Newtonian distribution, first proposed by Lees (1955). This may be written in the form

$$p'(\theta) = \begin{cases} (p'_0 - p'_\infty)\cos^2\theta + p'_\infty & \text{for} \quad |\theta| < \pi/2, \\ p'_\infty & \text{for} \quad \pi/2 \leqslant |\theta| < \pi, \end{cases} \tag{3.1}$$

where θ is the angle measured from the stagnation point, p_0 is the pressure at the stagnation point, and we have defined the pressure coefficient $p'_i = p_i / \frac{1}{2}\rho_\infty V^2$, the use of which is somewhat more convenient here than that of the usual pressure coefficient, C_p. For an inviscid perfect gas, p_0 is the pressure obtained by passing a free-stream flow through a normal shock, followed by an isentropic deceleration to stagnation conditions. If subscript 2 denotes conditions immediately behind the normal shock,

https://doi.org/10.1017/S0022112007007987 Published online by Cambridge University Press

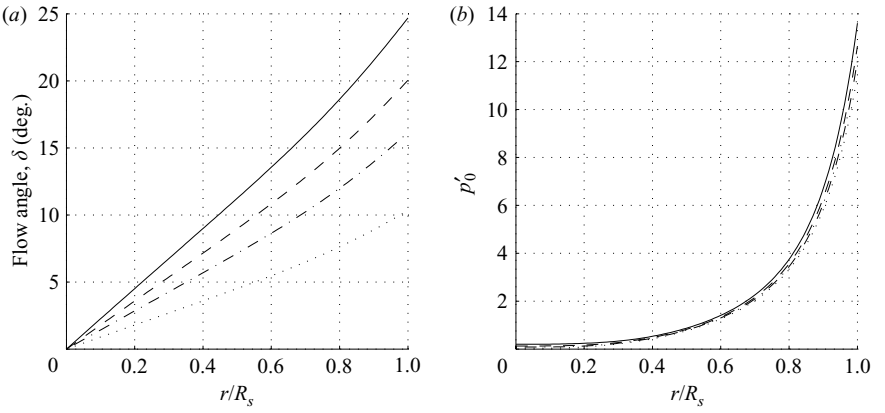


FIGURE 2. (*a*) Flow angle, δ, and (*b*) stagnation-point pressure coefficient, p_0', in the two-dimensional blast wave analogy: ——, $x/d_1 = 1$; – – –, $x/d_1 = 2$; – · –, $x/d_1 = 4$; · · ·, $x/d_1 = 16$.

then

$$\frac{p_0}{p_\infty} = \frac{p_2}{p_\infty}\frac{p_0}{p_2} = \left(1 + \frac{2\gamma}{\gamma+1}(M_\infty^2 - 1)\right)\left(1 + \frac{\gamma-1}{2}M_2^2\right)^{\gamma/(\gamma-1)}, \tag{3.2}$$

with

$$M_2^2 = \frac{(\gamma-1)M_\infty^2 + 2}{2\gamma M_\infty^2 - (\gamma-1)}. \tag{3.3}$$

We now consider the secondary cylinder inside the primary shocked region, denoting conditions in this region by the subscript 1. We use the above modified Newtonian description as our reference distribution, with p_1' replacing p_∞' in (3.1) and (3.2), and M_1 replacing M_∞ in (3.2) and (3.3). A further question arises here concerning the size of M_1. In particular, in the entropy wake, the Mach number is typically small as a result of the high temperatures in this region. Thus, even if M_∞ is large, M_1 is not necessarily so, and the modified Newtonian distribution may not be appropriate. Having already noted the questionable validity of our model in the entropy wake, however, we proceed with our formulation. We now make two modifications to our reference distribution in light of the altered flow conditions encountered by the secondary inside the shocked region.

First, we must account for the fact that the flow direction seen by the secondary is no longer aligned with that of the free stream, but is deflected by the primary bow shock. The flow angle resulting from this deflection, as given by the blast wave analogy, is shown in figure 2(*a*), plotted against the normalized lateral displacement, r/R_s, at various distances downstream. The ratio of specific heats used here is $\gamma = 1.4$, and this value will be assumed throughout this section. This deflection will have the effect of shifting the stagnation point to the inner side of the body, decreasing the drag slightly while providing a repulsive contribution to the lateral force, which we will equate with a positive lift contribution. Our choice of a circular cylinder becomes important at this point as the rotational symmetry possessed by this shape allows the modification to the reference distribution produced by this effect to be easily dealt with.

Secondly, we note from figure 2(*b*), in which the variable p_0' is plotted as a function of r/R_s at various distances downstream, that p_0' varies strongly with r/R_s. As R_s

https://doi.org/10.1017/S0022112007007987 Published online by Cambridge University Press

is a function of x, p_0' will vary with both x and r over the area covered by the cylinder. Note, in particular, that the effective stagnation pressure will be higher on the outer side of the cylinder than on the inner side, from which will arise an attractive contribution to the lateral force. We approximate this effect by Taylor-series expanding p_0 to the linear terms in x and r on the surface of the cylinder, giving an effective stagnation pressure of

$$p_0^{eff} = p_0 + \frac{1}{2}\frac{d_2}{d_1}\left(\frac{\partial p_0}{\partial(r/d_1)}\sin\theta + \frac{\partial p_0}{\partial(x/d_1)}\cos\theta\right). \tag{3.4}$$

In this expression, all lengths have been non-dimensionalized by the primary diameter d_1; the variables $\partial p_0/\partial(r/d_1)$ and $\partial p_0/\partial(x/d_1)$ may be determined by differentiating (3.2). It is not clear, however, that the x variations should be included with the r variations, as, given that the flow is primarily in the x-direction, it is not obvious that x variations can legitimately be localized in this manner. Also, given that the p_0' profiles in figure 2 vary only a small amount with downstream displacement and that R_s is a relatively weak function of x ($R_s \sim x^{2/3}$), x variations will be less significant than r variations. Thus, we shall include them here for the sake of completeness, but with the understanding that they are not crucial to our model.

Using these modifications to the reference distribution, we may write the drag and lift coefficients as

$$C_D = \frac{1}{2}\int_{-\pi/2}^{\pi/2}\left[p_0' - p_1' + \frac{1}{2}\frac{d_2}{d_1}\left(\frac{\partial(p_0'-p_1')}{\partial(r/d_1)}\sin(\theta-\delta) - \frac{\partial(p_0'-p_1')}{\partial(x/d_1)}\cos(\theta-\delta)\right)\right] \times \cos^2\theta\cos(\theta-\delta)\,\mathrm{d}\theta + \frac{1}{2}\int_{-\pi}^{\pi}\left[p_1' + \frac{1}{2}\frac{d_2}{d_1}\left(\frac{\partial p_1'}{\partial(r/d_1)}\sin(\theta-\delta) - \frac{\partial p_1'}{\partial(x/d_1)}\cos(\theta-\delta)\right)\right]\cos(\theta-\delta)\,\mathrm{d}\theta, \tag{3.5a}$$

$$C_L = -\frac{1}{2}\int_{-\pi/2}^{\pi/2}\left[p_0' - p_1' + \frac{1}{2}\frac{d_2}{d_1}\left(\frac{\partial(p_0'-p_1')}{\partial(r/d_1)}\sin(\theta-\delta) - \frac{\partial(p_0'-p_1')}{\partial(x/d_1)}\cos(\theta-\delta)\right)\right] \times \cos^2\theta\sin(\theta-\delta)\,\mathrm{d}\theta - \frac{1}{2}\int_{-\pi}^{\pi}\left[p_1' + \frac{1}{2}\frac{d_2}{d_1}\left(\frac{\partial p_1'}{\partial(r/d_1)}\sin(\theta-\delta) - \frac{\partial p_1'}{\partial(x/d_1)}\cos(\theta-\delta)\right)\right]\sin(\theta-\delta)\,\mathrm{d}\theta. \tag{3.5b}$$

These integrals may be evaluated to yield

$$C_D = \tfrac{2}{3}\cos\delta(p_0' - p_1') - \frac{\pi}{32}\frac{d_2}{d_1}\sin 2\delta\frac{\partial(p_0'-p_1)}{\partial(r/d_1)} - \frac{\pi}{16}\frac{d_2}{d_1}(2+\cos 2\delta)\frac{\partial(p_0'-p_1')}{\partial(x/d_1)} - \frac{\pi}{4}\frac{d_2}{d_1}\frac{\partial p_1'}{\partial(x/d_1)}, \tag{3.6a}$$

$$C_L = \tfrac{2}{3}\sin\delta(p_0' - p_1') - \frac{\pi}{32}\frac{d_2}{d_1}\sin 2\delta\frac{\partial(p_0'-p_1)}{\partial(x/d_1)} - \frac{\pi}{16}\frac{d_2}{d_1}(2-\cos 2\delta)\frac{\partial(p_0'-p_1')}{\partial(r/d_1)} - \frac{\pi}{4}\frac{d_2}{d_1}\frac{\partial p_1'}{\partial(r/d_1)}. \tag{3.6b}$$

https://doi.org/10.1017/S0022112007007987 Published online by Cambridge University Press

As the diameter ratio, d_2/d_1, is the only parameter we can freely choose in these coefficient expressions, it is of interest to determine the effect of varying this parameter. We are primarily interested in cases for which $d_2/d_1 < 1$, so, noting that over most of the shocked region $|\delta|$ is small and $p_0' \gg p_1'$ (and similarly with their respective derivatives), we may approximate the above formulae as

$$C_D \approx \tfrac{2}{3}\, p_0', \tag{3.7a}$$

$$C_L \approx \tfrac{2}{3}\, p_0' \sin\delta - \frac{\pi}{16}\frac{d_2}{d_1}\frac{\partial p_0'}{\partial (r/d_1)}. \tag{3.7b}$$

Equation (3.7*a*) is simply the drag coefficient in an undeflected uniform free stream. The behaviour of the approximate lift coefficient (3.7*b*) is potentially more interesting, however, as this expression contains two terms of opposite sign. As only the second term depends on body size, we have the potential for a qualitative change of behaviour as the body size is varied. In particular, there will be a tendency for the lift coefficient to become increasingly negative as the diameter ratio is increased. This may be understood physically to arise from the fact that the deflection of flow angle, which is responsible for the positive contribution to the lift coefficient, does not vary with body size, whereas for a larger secondary body, the difference in effective stagnation pressure from one side to the other will be greater, resulting in a larger negative contribution.

This body-size effect is observed in figure 3, in which the lift and drag coefficients – the full expressions, (3.6), rather than the approximations, (3.7) – are plotted for various diameter ratios and distances downstream. In addition to the variation of lift coefficient with body size, we also note a tendency for the lift coefficient to become more positive with increasing downstream displacement, indicating that the second term in (3.7*b*) decays more rapidly than the first. The drag coefficient, in contrast, depends only slightly on the diameter ratio and decreases in magnitude gradually as the downstream displacement is increased.

3.2. *Three-dimensional modelling*

In the three-dimensional case, we consider configurations involving two spheres. We proceed in a manner similar to the two-dimensional case, again seeking to approximate the pressure distribution on the secondary when it is inside the primary shocked region, the conditions of which are assumed to be given by the axisymmetric blast wave analogy. The modified Newtonian distribution on a sphere in a uniform free stream may be written

$$p'(\theta) = \begin{cases} (p_0' - p_\infty')\cos^2\theta + p_\infty' & \text{for} \quad \theta \in [0, \pi/2), \\ p_\infty' & \text{for} \quad \theta \in [\pi/2, \pi), \end{cases} \tag{3.8}$$

where θ is the zenith angle measured from the stagnation point and we have again defined the pressure coefficient $p_i' = p_i/\frac{1}{2}\rho_\infty V^2$. The variable p_0' may again be obtained from (3.2) and (3.3).

The flow angle and stagnation-point pressure profiles in the axisymmetric blast wave analogy are qualitatively similar to the analogous planar profiles seen in figure 2. We thus consider the same two modifications to the reference pressure distribution, namely the deflection in flow angle and the Taylor-expanded variation in effective stagnation pressure over the surface of the sphere. An additional complication is introduced in the three-dimensional case as isosurfaces in the blast-wave solution are now axisymmetric rather than planar. To make the coefficient integrals tractable,

https://doi.org/10.1017/S0022112007007987 Published online by Cambridge University Press

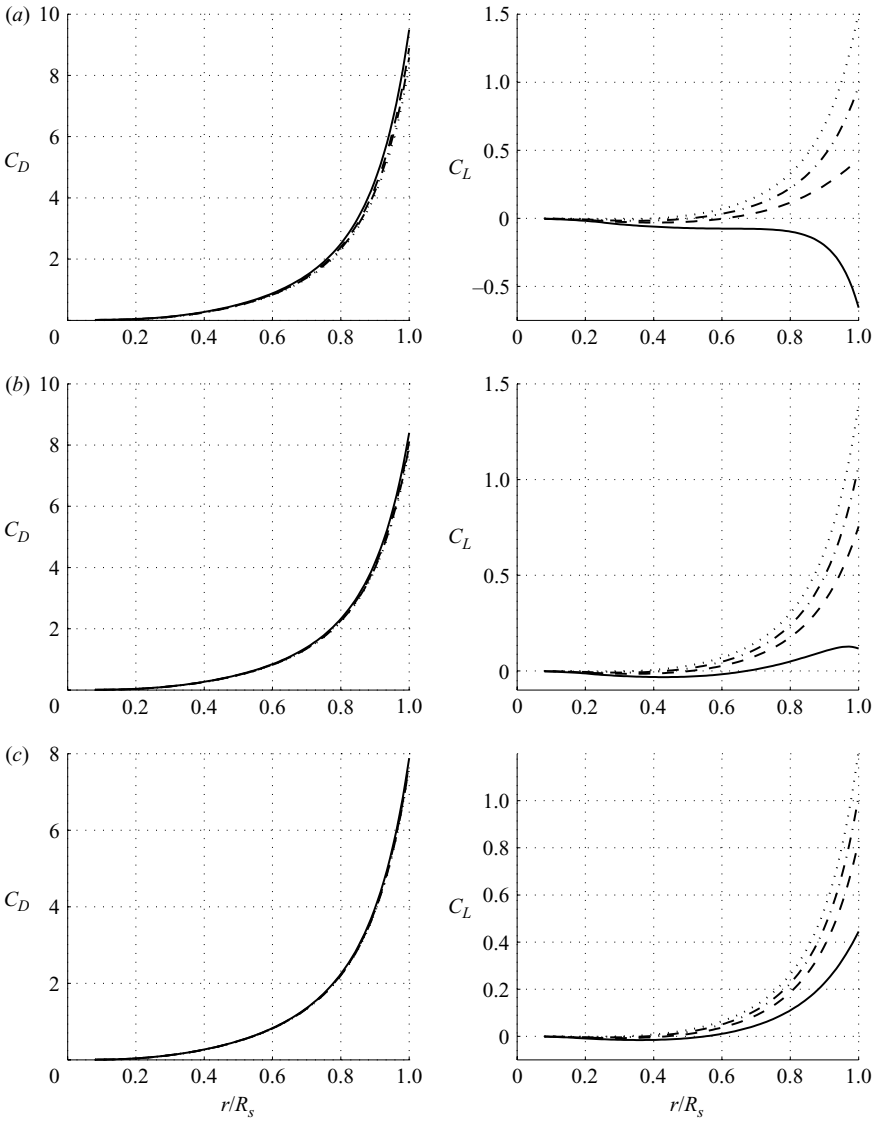


FIGURE 3. Theoretical force coefficients in two dimensions (including x-derivatives): ——, $d_2/d_1 = 1/2$; – – –, $d_2/d_1 = 1/3$; – · –, $d_2/d_1 = 1/4$; · · ·, $d_2/d_1 = 1/6$. (*a*) $x/d_1 = 2.5$, (*b*) 5, (*c*) 10.

however, we assume that these isosurfaces are locally flat over the volume occupied by the secondary. This is a reasonable approximation provided the lateral displacement of the secondary is large compared to the body radius.

Making use of Euler angles, and assuming without loss of generality that the direction of increasing lateral displacement is aligned with the positive lift axis, we may write the three-dimensional drag and lift coefficients as

$$C_D = \frac{1}{\pi}\int_0^{2\pi}\int_0^{\pi/2}\left[p_0' - p_1' + \frac{1}{2}\frac{d_2}{d_1}\left(\frac{\partial(p_0' - p_1')}{\partial(r/d_1)}\hat{r} - \frac{\partial(p_0' - p_1')}{\partial(x/d_1)}\hat{x}\right)\right]\cos^2\theta\,\hat{x}\sin\theta\,\mathrm{d}\theta\,\mathrm{d}\phi$$
$$+ \frac{1}{\pi}\int_0^{2\pi}\int_0^{\pi}\left[p_1' + \frac{1}{2}\frac{d_2}{d_1}\left(\frac{\partial p_1'}{\partial(r/d_1)}\hat{r} - \frac{\partial p_1'}{\partial(x/d_1)}\hat{x}\right)\right]\hat{x}\sin\theta\,\mathrm{d}\theta\,\mathrm{d}\phi, \qquad (3.9a)$$

https://doi.org/10.1017/S0022112007007987 Published online by Cambridge University Press

$$C_L = -\frac{1}{\pi}\int_0^{2\pi}\int_0^{\pi/2}\left[p_0' - p_1' + \frac{1}{2}\frac{d_2}{d_1}\left(\frac{\partial(p_0'-p_1')}{\partial(r/d_1)}\hat{r} - \frac{\partial(p_0'-p_1')}{\partial(x/d_1)}\hat{x}\right)\right]\cos^2\theta\,\hat{r}\sin\theta\,\mathrm{d}\theta\,\mathrm{d}\phi$$
$$-\frac{1}{\pi}\int_0^{2\pi}\int_0^{\pi}\left[p_1' + \frac{1}{2}\frac{d_2}{d_1}\left(\frac{\partial p_1'}{\partial(r/d_1)}\hat{r} - \frac{\partial p_1'}{\partial(x/d_1)}\hat{x}\right)\right]\hat{r}\sin\theta\,\mathrm{d}\theta\,\mathrm{d}\phi, \tag{3.9b}$$

where

$$\hat{r} = \cos\delta\sin\phi\sin\theta - \sin\delta\cos\theta,$$
$$\hat{x} = \sin\delta\sin\phi\sin\theta + \cos\delta\cos\theta.$$

These double integrals may be evaluated to yield

$$C_D = \tfrac{1}{2}\cos\delta(p_0' - p_1') - \frac{1}{15}\frac{d_2}{d_1}\sin 2\delta\frac{\partial(p_0'-p_1')}{\partial(r/d_1)}$$
$$-\frac{1}{15}\frac{d_2}{d_1}(2+\cos 2\delta)\frac{\partial(p_0'-p_1')}{\partial(x/d_1)} - \frac{2}{3}\frac{d_2}{d_1}\frac{\partial p_1'}{\partial(x/d_1)}, \tag{3.10a}$$

$$C_L = \tfrac{1}{2}\sin\delta(p_0' - p_1') - \frac{1}{15}\frac{d_2}{d_1}\sin 2\delta\frac{\partial(p_0'-p_1')}{\partial(x/d_1)}$$
$$-\frac{1}{15}\frac{d_2}{d_1}(2-\cos 2\delta)\frac{\partial(p_0'-p_1')}{\partial(r/d_1)} - \frac{2}{3}\frac{d_2}{d_1}\frac{\partial p_1'}{\partial(r/d_1)}. \tag{3.10b}$$

As in the planar case, we may approximate (3.10) by noting that $|\delta|$ is small and $p_0' \gg p_1'$, thus obtaining

$$C_D \approx \tfrac{1}{2}p_0', \tag{3.11a}$$

$$C_L \approx \tfrac{1}{2}p_0'\sin\delta - \frac{1}{15}\frac{d_2}{d_1}\frac{\partial p_0'}{\partial(r/d_1)}. \tag{3.11b}$$

These approximate expressions are similar in form to the corresponding planar expressions, and the same comments apply. In particular, we see again that the lift expression has two terms of opposite sign, only the second of which has a dependence on body size. Thus we again predict a qualitative change in lift behaviour as the diameter ratio is varied and this is seen in figure 4, in which the full formulae are plotted. While the effect of body size on the lift profiles is similar to that in the planar case, the downstream displacement effect does not carry over – while the magnitude of the lift value decreases as x/d_1 is increased, there is very little qualitative change. This difference is probably due to the $\partial p_0'/\partial(r/d_1)$ term in (3.7*b*) decaying more rapidly than that in (3.11*b*), as the shock radius grows more rapidly with increasing x in the former (planar) case.

Given the effect that has been observed of the diameter ratio on the lift coefficient, it is of interest to ask whether there is a critical ratio above or below which the lift experienced by the secondary body is exclusively of one sign within the shocked region. We thus set (3.10*b*) to zero and solve for d_2/d_1. The resulting curves, as functions of r/R_s, are shown in figure 5 for various distances downstream. These may be read in the following manner: at the given distance downstream, a secondary body for which the diameter ratio lies above the curve will experience a negative lift coefficient, and thus an attractive lateral force, whereas one lying below will experience a positive lift coefficient. We see that d_2/d_1 must be vanishingly small for the lift coefficient to be exclusively positive inside the shocked region, although for

https://doi.org/10.1017/S0022112007007987 Published online by Cambridge University Press

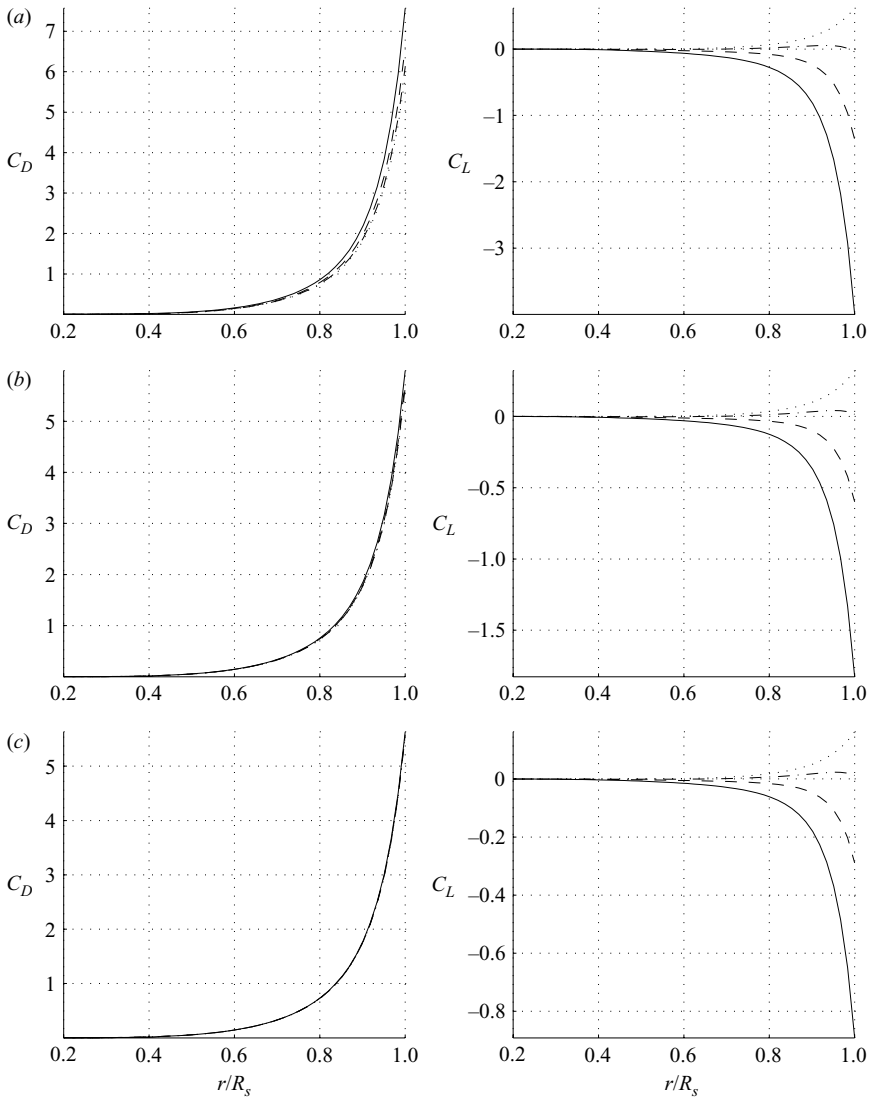


FIGURE 4. Theoretical force coefficients in three dimensions (including x-derivatives): ——, $d_2/d_1 = 1/2$; – – –, $d_2/d_1 = 1/4$; – · –, $d_2/d_1 = 1/8$; · · ·, $d_2/d_1 = 1/16$. (*a*) $x/d_1 = 2$, (*b*) 8, (*c*) 32.

a finitely small secondary, the region in which the lift coefficient is negative will be affected by the entropy wake, meaning our model is of questionable validity here. There does appear to be a finite value of d_2/d_1 above which the lift coefficient will be exclusively negative throughout the shocked region, however. This critical value is at $d_2/d_1 \approx 0.165$, i.e. a primary body approximately six times the diameter of the secondary body. A secondary body with a relative diameter larger than this value, if initially travelling within the shocked region with the same velocity as the primary body, is certain to be entrained, whereas smaller bodies have the possibility of being ejected from the shocked region by aerodynamic effects. Such a selection effect could have consequences, for example, on the distribution of fragments in a crater field resulting from the atmospheric breakup of a meteoritic body.

https://doi.org/10.1017/S0022112007007987 Published online by Cambridge University Press

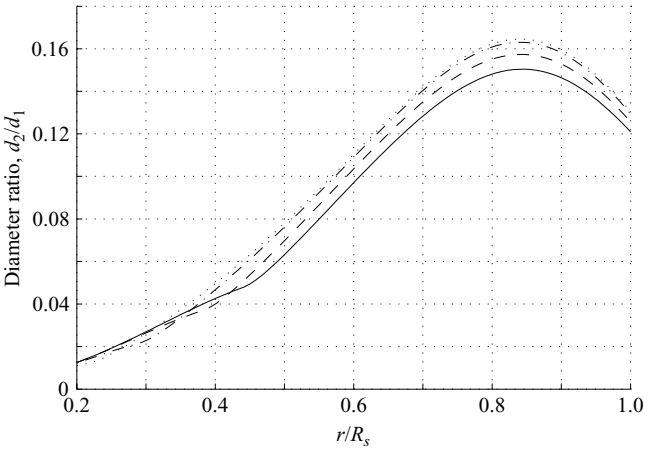


FIGURE 5. Diameter ratio in three dimensions at which a cross-over from a positive to a negative lift coefficient occurs: ——, $x/d_1 = 2$; – – –, $x/d_1 = 4$; – · –, $x/d_1 = 16$; · · ·, $x/d_1 = 64$.

4. Computational modelling

Computational modelling of the proximal bodies problem has been carried out in both two and three space dimensions using the AMROC (Adaptive Mesh Refinement in Object-oriented C++) software developed by Deiterding (2003). AMROC is a Cartesian adaptive mesh refinement (AMR) framework that implements the block-structured AMR algorithm after Berger & Colella (1988), designed specifically for the solution of hyperbolic fluid-flow problems, on distributed memory machines. Geometrically complex, possibly moving, boundaries are incorporated into simulations by employing a level-set-based ghost-fluid approach. Details of the boundary treatment and advanced verification and validation results for gaseous flows can be found, for instance, in Deiterding (2005). The framework architecture and the use of AMROC for fully coupled shock- and detonation-driven fluid–structure interaction problems is described in depth in Deiterding *et al.* (2005).

In order to provide direct comparisons with the analytical results of the previous section, simulated body geometries in the computations were limited to circular cylinders in the two-dimensional case and spheres in the three-dimensional case. In this section, we will outline the computational methodology and results, and comparisons with the analytical results will be given in the following section.

4.1. *Two-dimensional computational modelling*

All two-dimensional computations were carried out on the parallel compute cluster of the DOE ASC Alliance Center at the California Institute of Technology, consisting of 100 single processor Pentium-II nodes connected with Gigabit Ethernet. The Euler equations were solved for a perfect gas using a time-explicit finite-volume approach. The numerical flux was evaluated by employing the flux-vector splitting scheme after Van Leer within the second-order accurate MUSCL-Hancock slope-limiting technique. Godunov splitting was used for the multi-dimensional extension (cf. Toro 1999). In all computations described in this section, the free stream was at uniform conditions with a ratio of specific heats of $\gamma = 1.4$.

The parameters that were varied were the downstream and lateral displacements of the secondary cylinder, the free-stream Mach number, and the ratio of diameters of the two bodies. The runs were grouped according to the downstream displacement,

https://doi.org/10.1017/S0022112007007987 Published online by Cambridge University Press

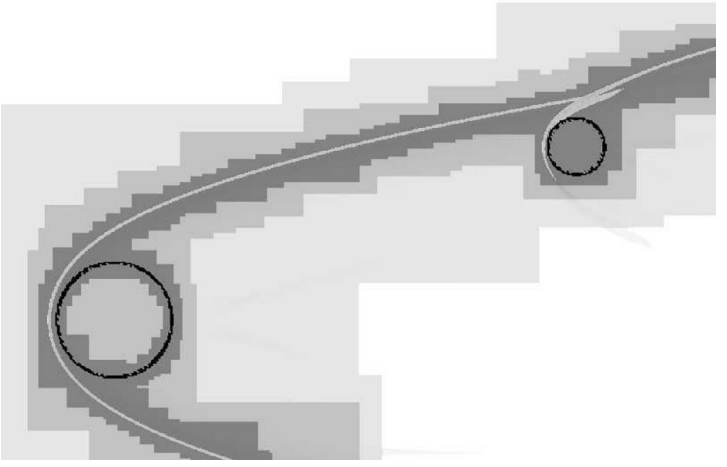


FIGURE 6. Visualization showing the refinement strategy used in the numerical simulations.

Mach number and diameter ratio, and for each combination of these, a series of simulations was performed in which the lateral position of the secondary body was varied incrementally from immediately behind the primary body to outside the primary bow shock. The lateral displacement was in the upwards direction, so a positive lift coefficient indicates a repulsive force from the plane of symmetry of the primary body.

Two values for each of the Mach number, the downstream displacement and the diameter ratio were chosen. Simulated Mach numbers were $M_\infty = 10$ and 50, with CFL numbers of 0.9 and 0.7, respectively. The downstream displacements used were 2 and 4 primary body diameters (centre-to-centre), with physical domains of 5.2×5.2 and 8.3×7.3 primary diameters, respectively. The corresponding base grids were 200×200 and 320×280. The values of the diameter ratio simulated were $d_2/d_1 = 1/2$ and $1/6$.

Two additional levels of dynamic isotropic mesh refinement, each with a refinement factor of 2, were allowed. Note that in AMROC, mesh adaptation is realized by clustering several finite-volume cells, requiring refinement into larger, succesively embedded, rectangular blocks of uniformly refined step size. Characteristic of the Berger & Colella approach is that spatial and temporal mesh widths are refined equally, leaving the CFL number (in principle) unaltered.

The refinement indicator for the dynamic mesh adaptation was the scaled gradient of the density. The boundaries of the embedded bodies were always refined up to the highest level, resulting in an effective resolution of 154 cells for the primary body. The refinement strategies were similar in two and three dimensions – a visualization of a three-dimensional case (corresponding to the schlieren image seen in figure 8) is shown in figure 6. Depicted are the successively embedded domains of the three levels of additional refinement (shaded grey), together with the static sphere boundaries (black). For reference, the primary and secondary bow shocks are shown as light grey on the highest refinement level.

All permutations of the indicated choices of problem parameters were simulated. Using 12 nodes, the compute time was typically 40 h CPU for a run on the physically smaller grid and 60 h CPU for the larger grid, corresponding to 3.3 and 5 h wall clock time, respectively.

https://doi.org/10.1017/S0022112007007987 Published online by Cambridge University Press

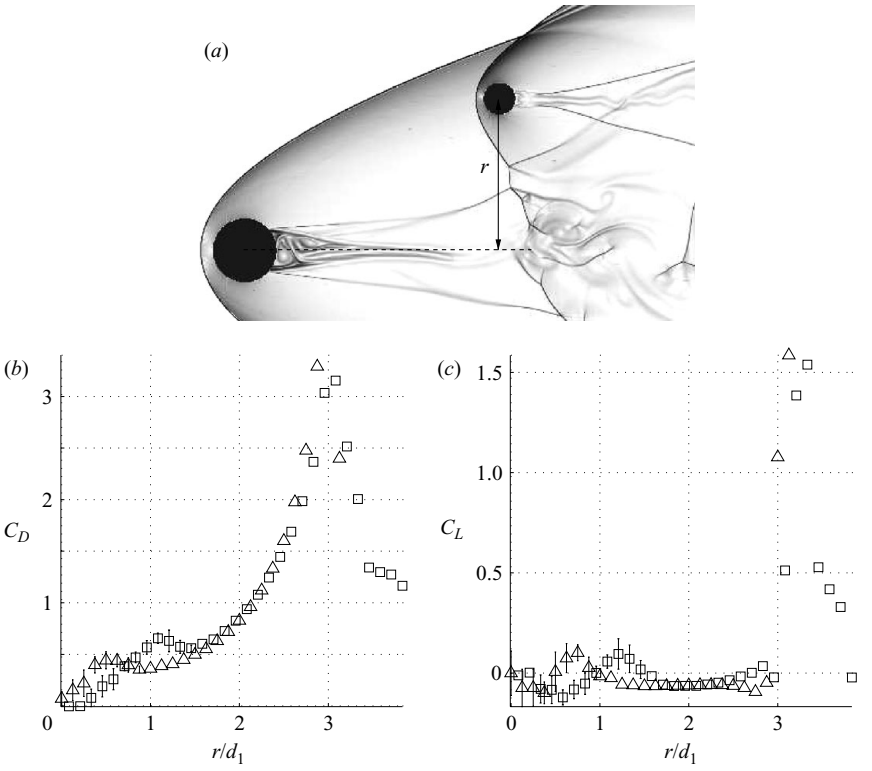


FIGURE 7. (b, c) Secondary force coefficients obtained from a set of two-dimensional numerical simulations, a schlieren image from one of which is shown in (a). The lateral displacement is normalized by the primary diameter, d_1. The downstream displacement, centre-to-centre is $4d_1$ and the diameter ratio is 1/2: □, $M_\infty = 10$; △, $M_\infty = 50$. The Mach number in the schlieren image is $M_\infty = 50$.

To generate the flow in a given run, the velocity at the inlet boundary was ramped up at constant density and pressure to the appropriate steady value. The lift and drag values on each body were calculated on-the-fly by evaluating numerically the surface integral of hydrodynamic pressure forces over the body. In the case of the $M_\infty = 10$ simulations, steady flow at the inlet boundary was established from $t = 0.25$, where t is the computational time variable. One unit of computational time corresponded to the physical time necessary for the free stream to cover approximately 21 primary diameters. Quasi-steady flow over the bodies (as determined from the force coefficient profiles) was typically achieved by $t \approx 1$. The simulations were continued until $t = 3.0$, with the mean lift and drag values calculated from $t = 2.1$. For the $M_\infty = 50$ simulations, this time scale was compressed by a factor of 5. In either case, each simulation typically involved 3000 to 4000 time steps.

Figure 7 shows the force coefficients obtained from a given set of simulations, with the parameters indicated in the caption. A computational schlieren image from one of the simulations in this set is also shown. Error bars, indicating the standard deviation in the relevant coefficient, are plotted for those cases in which the drag deviation is more than 5 % of the mean value. As may be seen, this occurs exclusively at small values of r/d_1 ($r/d_1 \lesssim 1.5$) and is caused by unsteadiness in the flow produced by interactions of the secondary with either the wake region or the separation shock from

https://doi.org/10.1017/S0022112007007987 Published online by Cambridge University Press

Downstream displacement	1.5	1.5	1.5	4
Mach number	10,50	10	50	10,50
Diameter ratio (d_2/d_1)	1/2	1/4,1/8	1/4	1/2
Base grid	$40 \times 40 \times 32$	$40 \times 48 \times 48$	$40 \times 48 \times 48$	$64 \times 56 \times 32$
Additional refinement	2,2,2	2,2,4	2,2,4	2,2,2
Physical domain	$3.9 \times 3.9 \times 3.1$	$3.9 \times 4.7 \times 4.7$	$3.9 \times 4.7 \times 4.7$	$6.4 \times 5.5 \times 3.1$

TABLE 1. Details of the three-dimensional computations. The downstream displacements are the centre-to-centre values; both these and the physical domains are given in terms of the primary diameter.

the rear of the primary. As the lateral displacement is increased, we see that the drag rises in a manner similar to that observed in the analytical profiles. Meanwhile, the lift remains at small largely negative values until the primary shock begins to impinge upon the secondary at $r/d_1 \approx 3$. At this point, the lift jumps sharply to positive values, for reasons outlined in § 1. As the secondary clears the primary bow shock, the drag and lift coefficients drop to their respective free-stream values of ≈ 1.2 and 0. The most notable difference between the two Mach numbers is in the location of the hump observed in all the profiles at small r/d_1. This feature in each case results from the interaction of the secondary with the separation shock, which lies at smaller r/d_1 for larger Mach numbers. Otherwise, the profiles from the two Mach numbers differ relatively little, indicating that the hypersonic Mach number independence principle holds reasonably well at this point downstream for Mach numbers $\gtrsim 10$.

4.2. *Three-dimensional computational modelling*

A series of three-dimensional numerical simulations was carried out on the IBM Power4+ machine DataStar at the San Diego Supercomputing Center. The flow over two spheres was simulated by solving the three-dimensional Euler equations for a perfect gas with the numerical techniques outlined in the previous section.

The parameters that were varied were the same as in the two-dimensional case, namely the downstream and lateral displacements of the secondary body, the diameter ratio, and the Mach number. Table 1 gives an overview of the combinations of parameters that were simulated, along with some details of the computations. Larger computational domains were used for smaller secondary bodies because, in these simulations, a number of secondaries were simulated in a given run. These were each at different lateral displacements, and sufficiently spaced that they did not interact aerodynamically with one another. The additional refinement entry indicates the isotropic refinement factor for each additional level: thus, three additional refinement levels were used in each case, although the refinement factor at the highest level varied. The primary body had an effective resolution of either 82 or 164 cells, the latter being the case in the more refined simulations. The CFL number in all three-dimensional simulations was 0.8, with typically around 1500 time steps computed. Computational costs were typically 1000 h CPU using either 48 or 64 processors for the less refined simulations and 4000 h CPU on 64 processors for the more refined simulations (corresponding to 62.5 h wall clock time).

The generation of the flow and the calculation of the force coefficients were carried out in an analogous manner to the two-dimensional simulations. Although the inlet-flow time scales were similar to those in two dimensions, it was found that a quasi-steady flow over the two bodies took somewhat longer to establish here, and so the mean coefficients were calculated over a somewhat shorter time period – typically

https://doi.org/10.1017/S0022112007007987 Published online by Cambridge University Press

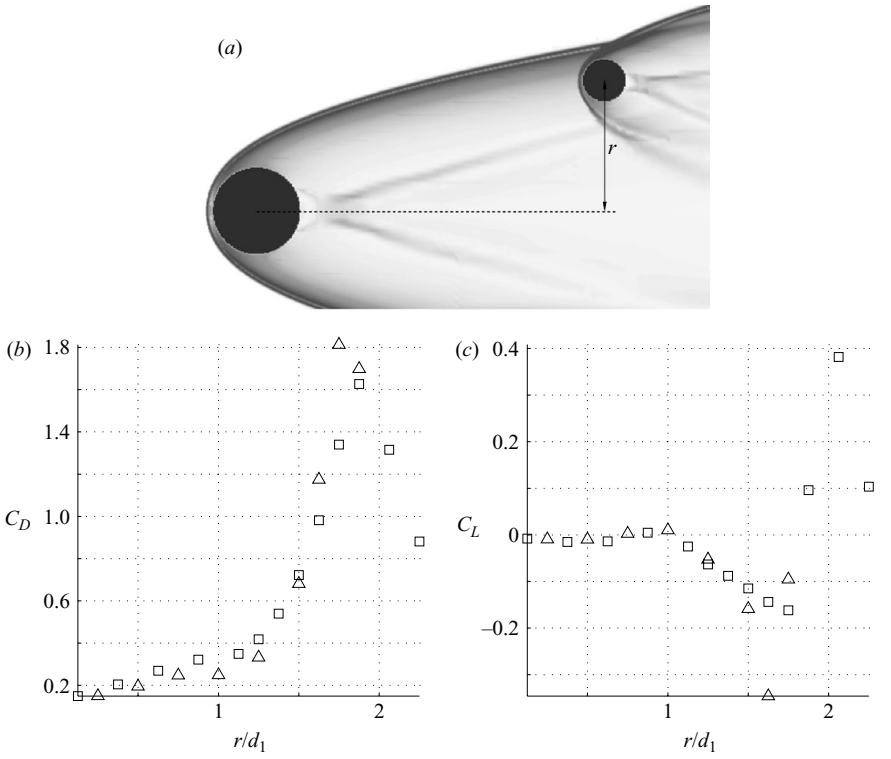


FIGURE 8. (b, c) Secondary force coefficients obtained from a set of three-dimensional numerical simulations, a schlieren image from one of which is shown in (a). The downstream displacement, centre-to-centre is $4d_1$ and the diameter ratio is $1/2$: □, $M_\infty = 10$; △, $M_\infty = 50$. The Mach number in the schlieren image is $M_\infty = 50$.

the last 10 % of the total computational time, corresponding to a physical flow time necessary for the free stream to cover approximately 10 primary body diameters.

Figure 8 shows the force coefficients from a group of three-dimensional simulations as functions of the lateral displacement, with a schlieren image taken from one of these also shown. The choice of parameters for this group is indicated in the caption. The profiles are qualitatively similar to those seen in the two-dimensional case and most of the same comments apply. Note, however, that the unsteadiness in the wake region is typically much smaller here than in two dimensions. In all simulations shown, the standard deviation in the drag value over the averaging period was less than 2 % of the mean value. This may be attributed to the fact that the features that give rise to this variation, such as the separation shock from the rear of the primary, decay more rapidly in the downstream direction in the three-dimensional case.

We do observe a somewhat larger difference between the two Mach number profiles than was seen in the two-dimensional case, indicating that the Mach number independence principle is more questionable here (the downstream displacements are the same in both cases). This is to be expected, however, since in three dimensions the shock angle, β, is shallower, and so at equal distances downstream the assumption of a large normal shock Mach number, $M_\infty \sin\beta$, on which this principle relies is more tenuous.

https://doi.org/10.1017/S0022112007007987 Published online by Cambridge University Press

Additional levels of refinement	C_D	ΔC_D	C_L	ΔC_L
0	2.051		−0.051	
1	2.117	0.066	−0.128	−0.077
2	2.320	0.203	−0.228	−0.100
3	2.346	0.026	−0.183	0.045

TABLE 2. C_D and C_L values for the two-dimensional refinement study. Δ indicates the difference between the values at current and previous levels of refinement.

4.3. *Refinement studies*

To assess the accuracy of the computational method, two- and a three-dimensional mesh refinement studies have been carried out. In each case, a particularly sensitive combination of physical problem parameters was chosen to provide practical upper bounds. In order to obtain directly applicable results, the refinement studies were not carried out on uniform grids, but employed dynamic mesh adaptation with the same refinement parameters as described above.

4.3.1. *Two dimensions*

Table 2 contains the results of the two-dimensional refinement study. The choice of parameters for this study was as follows: the downstream and lateral displacements of the secondary body were both 2 primary body diameters, the diameter ratio was 1/2, and the Mach number was 10. In this configuration, complex shock interactions were observed between the secondary and primary bow shocks ahead of the secondary body. The calculated forces on the secondary could therefore be expected to be sensitive to shock position alterations resulting from increases in the effective mesh resolution.

Up to three additional levels of refinement over the base grid were used, each with a refinement factor of 2. The C_D and C_L values are given in each case, as well as the change in value from that at the previous level of refinement. The coefficients do appear to be converging, but are indeed quite sensitive. Between the two highest refinement levels, the changes in the drag and lift are $\sim 1\,\%$ and $\sim 2\,\%$ of the drag value, respectively. We would expect the majority of configurations to be significantly less sensitive to resolution changes than the current one, however.

4.3.2. *Three dimensions*

The choice of parameters for the three-dimensional refinement study was downstream and lateral displacements of $1.5d_1$ and $1.25d_1$ respectively, a diameter ratio of 1/2, and a Mach number of 10. This combination was selected because, as in the two-dimensional case, shock interactions are clearly present in this configuration. In this case, the primary bow shock impinges directly upon the secondary: as may be seen in the analogous area of figure 8 ($1.6 \lesssim r/d_1 \lesssim 2.0$), such impingement results in large gradients in the force coefficient profiles. Resolution changes can thus be expected to have a major influence on the force evaluation.

Simulations were carried out for one to four levels of additional refinement (always of refinement factor 2) over the base grid (table 3). The values are converging, but again the lift especially is sensitive to changes in refinement level. Visualizations of these simulations show that increasing the effective resolution causes a slight decrease in the primary bow shock radius, or, alternatively, a small increase in the effective

https://doi.org/10.1017/S0022112007007987 Published online by Cambridge University Press

Additional levels of refinement	C_D	ΔC_D	C_L	ΔC_L
1	1.264		−0.176	
2	1.442	0.178	−0.019	0.157
3	1.423	−0.019	0.052	0.071
4	1.408	−0.015	0.087	0.035

TABLE 3. C_D and C_L values for the three-dimensional refinement study.

lateral displacement of the secondary body. This is consistent with the more positive lift values observed at higher levels of refinement.

The computation with four additional levels required approximately 35 000 h CPU and took approximately 10 days wall clock time to complete on 144 processors. Thus, given current computing performance, the maximal number of additional levels that can realistically be used is three. From table 3, we estimate the maximal errors in drag and lift at this level of resolution to be $\sim$2 % and $\sim$5 %, respectively, of the mean drag value. Note that these errors will be smaller, however, in configurations that are less sensitive to changes in shock position.

5. Comparison of theoretical and computational results

5.1. *Two dimensions*

In figure 9, the two-dimensional drag and lift coefficients obtained with the analytical methodology of § 3.1 are compared with those obtained from two-dimensional computations for various choices of the downstream displacement and the diameter ratio.

Theoretical profiles both with and without x-derivatives are included, as are the computational values obtained at both $M_\infty = 10$ and 50. The lateral displacement has been normalized in each case by the corresponding shock radius – in the theoretical cases this may be obtained directly, whereas the computational radii were estimated from visualizations of the flow. In each case, the downstream displacement is the centre-to-centre value: the shock stand-off distance was also estimated from visualizations in order to allow the calculation of an appropriate x/d_1 value for the analytical model.

We first note that agreement for r/R_s close to either 0 or 1 is generally poor. This is to be expected, however, as near $r/R_s = 0$, the secondary body in the numerical simulations interacts with the primary body wake region and separation shock, neither of which is present in the blast wave analogy. At slightly larger r/R_s, the influence of the blast-wave entropy wake will also be present. Similarly, as r/R_s approaches 1, the secondary begins to interact with the primary bow shock, and the analytical model is no longer valid. Away from these two extremes, however, the computational trends are reasonably well captured by the theory. The body-size effect that was noted earlier in the analytical model is also present in the numerical simulations, and is well-predicted by the model. There is generally little to choose between the profiles with and without x-derivatives, although those that include these terms do show a slight tendency to overestimate the drag coefficient value.

5.2. *Three dimensions*

In figure 10, a comparison is made between the three-dimensional theoretical and computational coefficients, with the lateral displacements again having been

https://doi.org/10.1017/S0022112007007987 Published online by Cambridge University Press

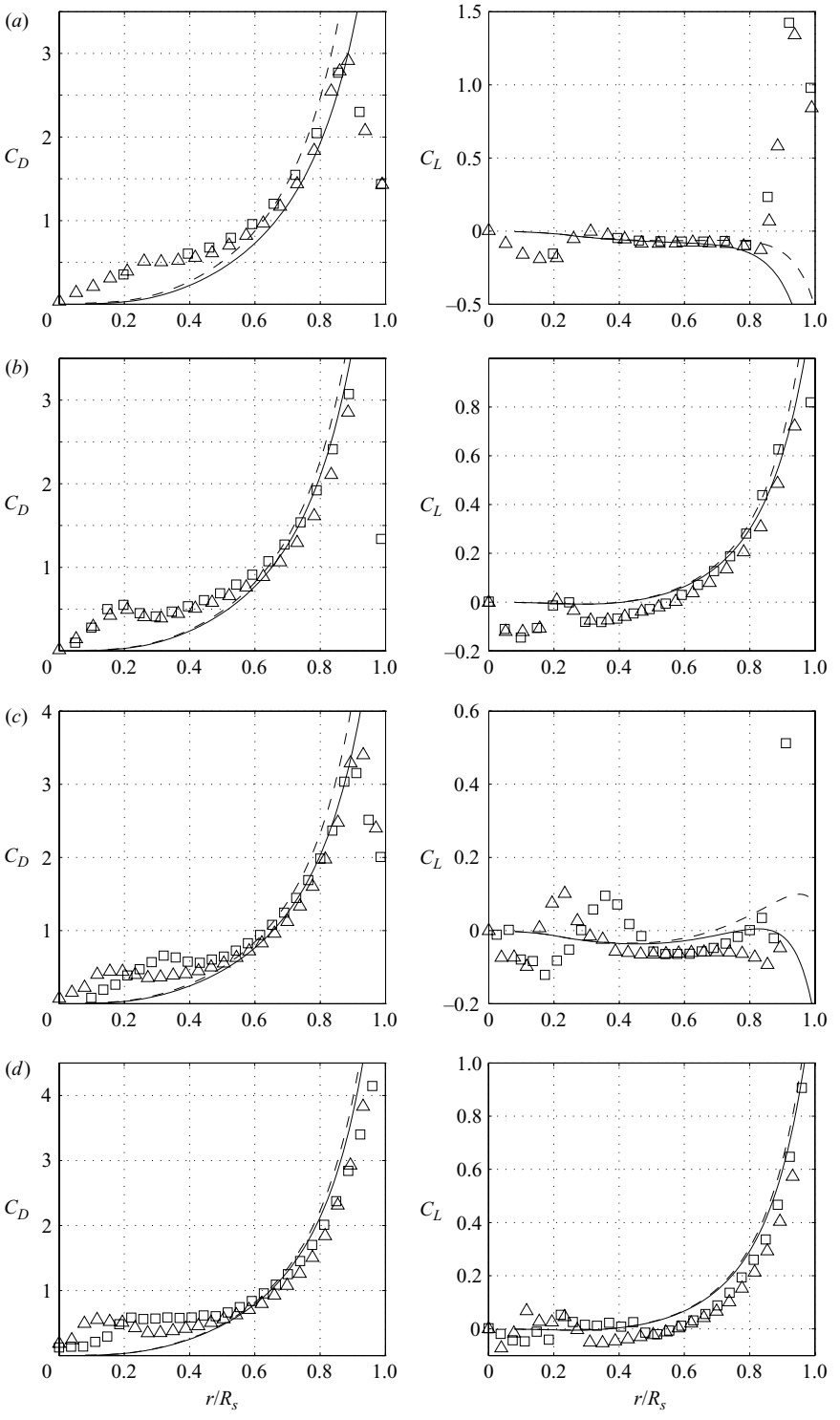


FIGURE 9. Comparison of theoretical model with computations in two dimensions: ——, theoretical without x-derivatives; – – –, theoretical with x-derivatives; □, computational, $M_\infty = 10$; △, computational, $M_\infty = 50$. Downstream displacement (a, b) 2 primary diameters, (c, d) 4 primary diameters. Diameter ratio (a, c) 1/2; (b, d) 1/6.

https://doi.org/10.1017/S0022112007007987 Published online by Cambridge University Press

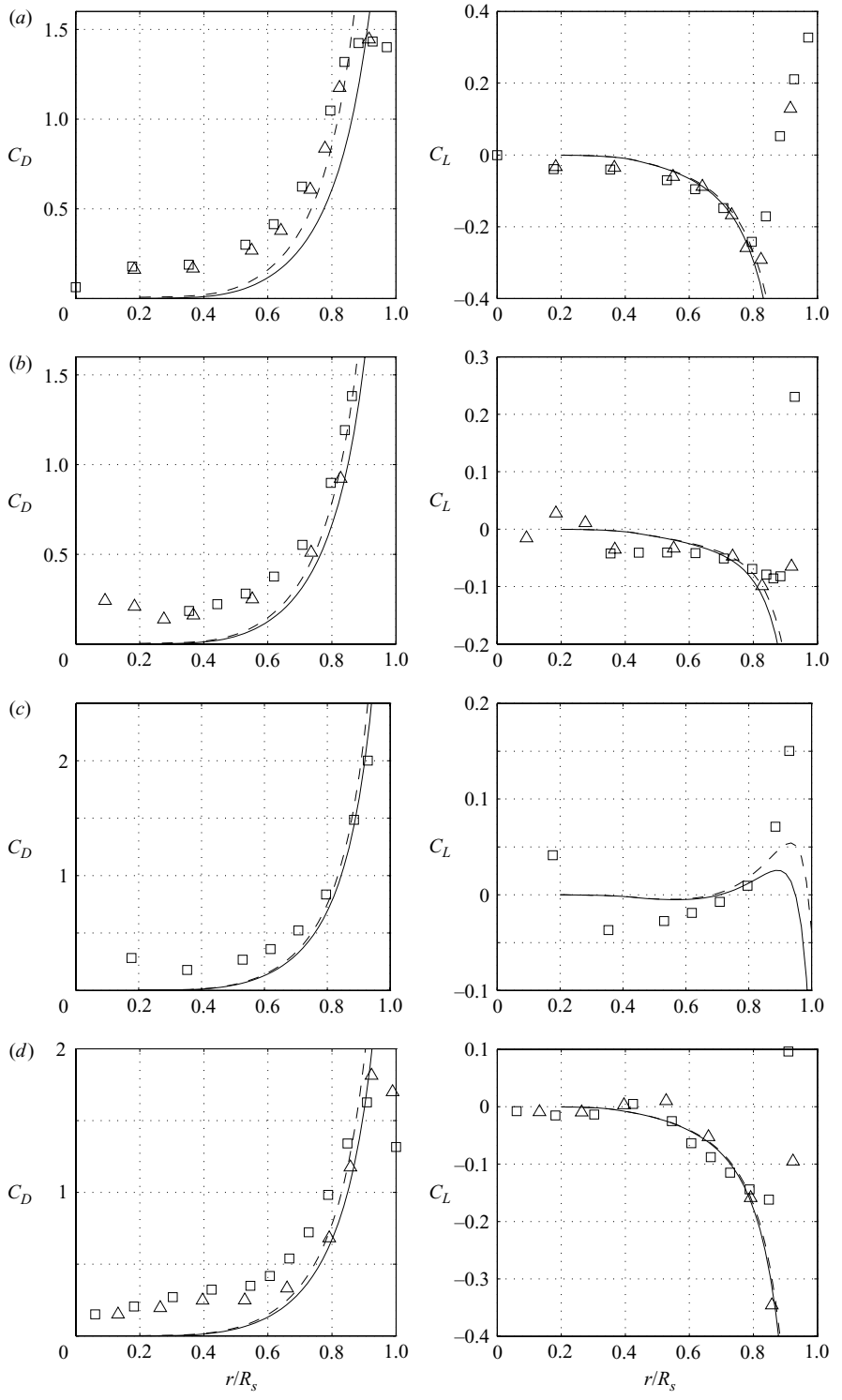


FIGURE 10. Comparison of theoretical model with computations in three dimensions: ——, theoretical without x-derivatives; – – –, theoretical with x-derivatives; □, computational, $M_\infty = 10$; △, computational, $M_\infty = 50$. Downstream displacement (a–c) 1.5 primary diameters, (d) 4 primary diameters. Diameter ratio (a, d) 1/2; (b) 1/4; (c) 1/8.

https://doi.org/10.1017/S0022112007007987 Published online by Cambridge University Press

normalized by the relevant shock radii. The same comments as in the two-dimensional case apply for r/R_s close to either 0 or 1. In general, however, agreement for intermediate values of r/R_s is not as good: in particular, the theoretical drag coefficient profiles drop off somewhat more rapidly with decreasing r/R_s than do the computational values. The influence of the entropy wake thus appears to be more prominent here, and this results in the variable p_0' decaying more quickly in the theoretical model than is physically realistic. The ability of the model to predict the lift coefficients for intermediate values of r/R_s is surprisingly good, however, with the body-size effect again accurately described. In contrast to the two-dimensional case, the profiles that include x-derivatives show slightly better agreement than those without. Also, as might be expected, the theory is better able to predict the $M_\infty = 50$ values than those at $M_\infty = 10$.

5.3. *Shock radius discrepancy*

As noted previously, all lateral displacements in the coefficient profiles presented in this section have been normalized by the relevant shock radius, theoretical or computational. There was, however, a significant discrepancy between the theoretical and computational shock radii in all cases, with the theoretical value being consistently lower. This discrepancy is well understood, however, as arising from the assumption of a point generation of energy in the blast-wave analogy. In any physical situation, the flow energy is produced over the finite area of the body surface, and this results in the shock radius being displaced outwards from the blast-wave value.

This discrepancy does limit the predictive power of the theoretical model somewhat, as the actual shock radius must be known before the model may be reasonably applied. However, a single experiment or computation with only the primary body present would suffice to obtain the shock radius at all distances downstream of interest, and the analytical model could then be applied with this knowledge.

Alternatively, several authors have proposed empirical correlations to the shock shape produced by a blunt body based on experimental data (see, e.g. Ambrosio & Wortman 1962; Billig 1967). The shapes given by these correlations are surprisingly accurate, and could be used to provide a more accurate shock radius to which the methodology could be applied. Another alternative would be to introduce the concept of an effective origin for the shock radius in the far field that would be displaced outwards relative to the axis of symmetry. For the current spherical geometry, for example, it was found that for large Mach numbers ($M_\infty \gtrsim 50$) a displacement of approximately a quarter of the primary sphere diameter would give much improved agreement with the computational shock radius.

6. Experimental investigation

6.1. *The T5 hypervelocity shock tunnel*

A series of experiments has been performed in the T5 hypervelocity shock tunnel at the California Institute of Technology to determine the forces on the secondary body in several spherical proximal body configurations. The T5 is a free-piston driven, reflected shock wind tunnel, capable of producing flow speeds of up to $6\,\mathrm{km\,s^{-1}}$ for test times of millisecond duration. The facility is illustrated schematically in figure 11, and further details may be found in Hornung *et al.* (1991).

The test gas in all experiments was carbon dioxide, chosen to maximize the test time length and minimize the amount of luminosity produced during each shot. All experiments were performed at nominally the same test condition, but there

https://doi.org/10.1017/S0022112007007987 Published online by Cambridge University Press

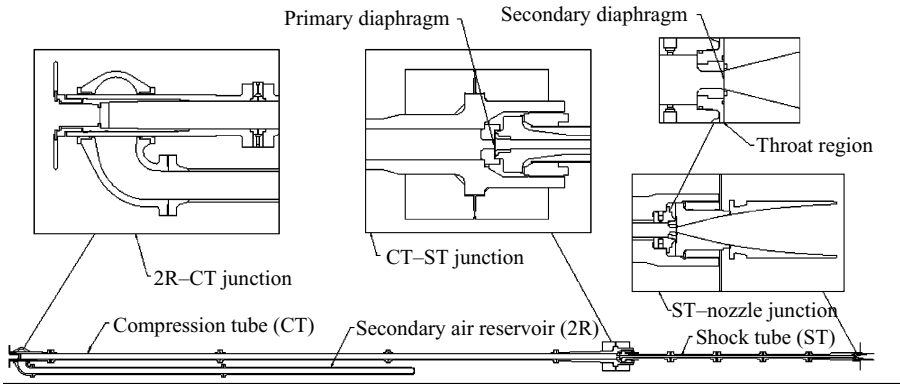


FIGURE 11. Vertical cross-section of the T5 facility, with enlargements of the junctions between major components. A contoured nozzle is shown, but in all experiments described here the nozzle geometry was conical, with an area ratio of 100.

was some variation in reservoir and free-stream conditions between shots owing to differences in the primary diaphragm burst pressure. For each shot, reservoir conditions were calculated from measured pressures and the incident shock speed using ESTC (Equilibrium Shock Tube Calculation), due to McIntosh (1969). Free-stream conditions were then calculated at the relevant point downstream with NENZF (Non-Equilibrium NoZzle Flow), due to Lordi, Mates & Moselle (1966). Representative values for the reservoir pressure and enthalpy were 17 MPa and 9.4 MJ kg^{-1}, while the free-stream velocity, density and Mach number were typically 3100 m s^{-1}, 0.035 kg m^{-3} and 4.5, respectively.

6.2. *Experimental set-up*

A schematic of the apparatus for this series of experiments is shown in figure 12. The primary sphere, of diameter 63.5 mm, was mounted rigidly to the test section by means of a sting and supporting plates. The mounting mechanism allowed for changes in the vertical and horizontal positions of the primary sphere. The secondary sphere, of diameter 32 mm, was suspended from the roof of the test section by two cotton threads in a V-arrangement. At the beginning of each shot, the cotton threads were destroyed by the onset of the flow, allowing for free-floating model behaviour during the test time.

A catcher mechanism consisting of a bent hollow tube was mounted directly behind the secondary sphere. The purpose of this device was two-fold: first, it served to terminate the sphere motion after the conclusion of the steady-flow period, preventing the accumulation of a velocity sufficient to damage the model or the internal instrumentation. Rubber padding on the face of the catcher lessened the resulting impact. Secondly, in those experiments in which an accelerometer was mounted inside the secondary sphere, the catcher provided a path by which the accelerometer cable could leave the test section without being exposed to the hostile flow environment. Further protection was provided in the relevant shots by a thin metal tube that was attached to the rear of the sphere. This tube was initially positioned so that it could move unimpeded into the hole in the centre of the catcher, and ensured that the sphere was guided towards the catcher after the test time.

The presence of the catcher might be expected to influence the measured forces, given that the existence of subsonic regions in the secondary wake allows the

https://doi.org/10.1017/S0022112007007987 Published online by Cambridge University Press

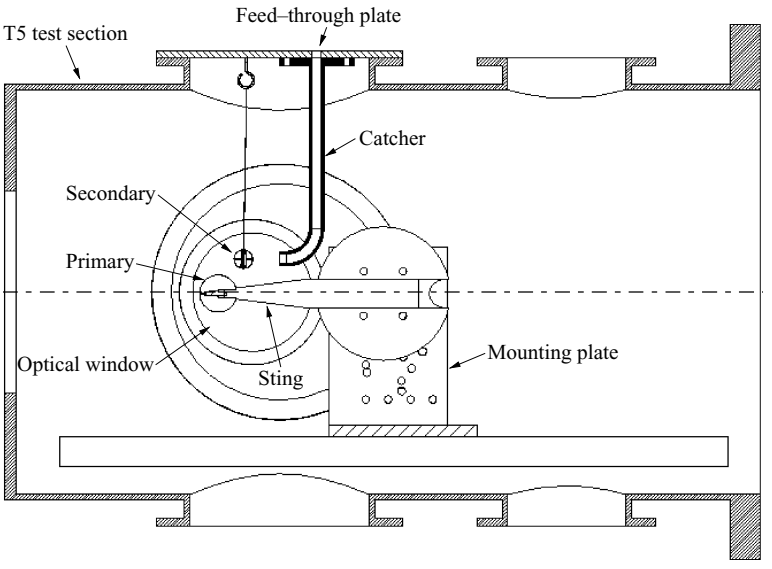


FIGURE 12. Arrangement of apparatus in the T5 test section (to scale). The scale relative to the facility may be gauged by comparing the nozzle opening in the left-hand wall of the test section with the nozzle in figure 11.

propagation of information upstream from the catcher, affecting the flow on the rear of the body. Numerical simulations were performed in order to investigate this effect. The flow over a sphere in a uniform perfect gas free stream of appropriate Mach number and ratio of specific heats was simulated, both with and without a cylindrical body of the same relative size as the catcher present. It was found that the inclusion of the catcher led to a slight shift in the separation point from the rear of the sphere, and a resulting decrease in the drag by approximately 2 %. Although these simulations give only an indication of the influence of the catcher in proximal configurations, the percentage change in the drag value is unlikely to exceed this amount. Also, the effect on the lift is likely to be small, given the negligible contribution to the lift from the rear part of the sphere.

6.3. *Measurement techniques*

Two means of force-measurement were employed in this series of experiments. In both cases, the quantities measured were accelerations (indirectly in the first case, directly in the second), with the relevant forces being easily obtained from these.

The first means of measuring the secondary forces was through images obtained from high-speed digital cinematography. The optical system employed was a conventional Z-arrangement schlieren: a Vision Research Phantom v5 digital camera was used in conjunction with a continuous white light source to record a sequence of schlieren images during each shot. The resolution was either 256×128 or 256×64 pixels, with the frame rate set to the maximum value in each case of 25 000 or 38 000 frames per second, respectively.

The first step in deriving secondary acceleration values from the images obtained in a given shot was the construction of displacement profiles in the drag and lift directions. To this end, each image in the sequence was processed by an edge-detection routine, and a circle was fitted in the least-squares sense to the locus of edge points corresponding to the secondary body. This gave the x and y coordinates

https://doi.org/10.1017/S0022112007007987 Published online by Cambridge University Press

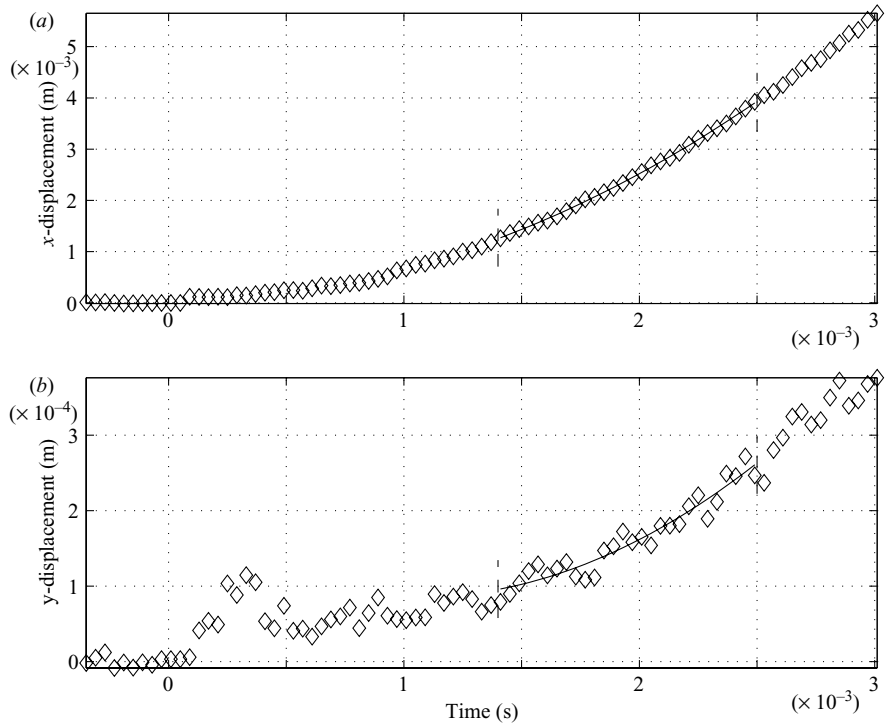


FIGURE 13. Displacement profiles of the secondary body in the (*a*) drag and (*b*) lift directions during T5 shot 2330: ◇, model locations; —, fitted quadratic polynomial. Resulting accelerations (*a*) $x = 1310 \pm 93\ \mathrm{m\,s^{-2}}$; (*b*) $y = 168 \pm 59\ \mathrm{m\,s^{-2}}$.

of the body, together with the scaling factor that transformed from image to physical dimensions.

To determine the drag and lift accelerations from the trajectory thus obtained, it was assumed that these were constant over the steady test time. This allowed quadratic polynomials to be fitted in the least-squares sense to each of the x and y displacement profiles as functions of time, with the acceleration in each case being given simply by twice the quadratic coefficient. The error in each of the fits was estimated from the residuals in a manner described by Meyer (1975). An example of this process is shown in figure 13. Each of the x and y displacement profiles are plotted as a function of time, with the curve given by the least-squares fit over the steady flow time shown by the solid line, and the resulting accelerations indicated in the caption.

Note that the total motion of the sphere during the test time is less than 3 mm, meaning that our assumption of a fixed physical configuration during the test time is reasonable. Also, the maximum velocity achieved during this time is approximately $10\ \mathrm{m\,s^{-1}}$, which is negligible compared to the flow velocity.

The second means of measuring the drag force on the secondary sphere was through direct measurements of the acceleration by an internally mounted uniaxial accelerometer. This method was not used in all of the experiments in the current series, however, for the following reasons. The first experiment in this series, T5 shot 2322, was a validation experiment in which the secondary sphere was situated outside the primary shock, and thus exposed to the uniform free stream. In this experiment, good agreement was observed between the drag values obtained from the accelerometer

https://doi.org/10.1017/S0022112007007987 Published online by Cambridge University Press

Shot number	Axial displacement	Lateral displacement	Shock position	Experimental		Computational	
				C_D	C_L	C_D	C_L
2322	–	–	Sphere outside	0.97 ± 0.07	(accelerometer)	0.956	(perfect gas)
				0.95 ± 0.07	(images)	0.995	(real gas)
2326	1.07	1.21	Impinging upper	1.44 ± 0.09	0.02 ± 0.11	1.40	0.23
2327	1.25	1.18	Just impinging	1.43 ± 0.11	(accelerometer)	1.34	
2328	1.25	1.18	Just impinging	1.35 ± 0.11	0.07 ± 0.11	1.34	0.01
2329	1.50	1.21	Sphere inside	1.08 ± 0.15	-0.13 ± 0.09	1.05	-0.05
2330	1.50	1.67	Impinging lower	1.11 ± 0.08	0.29 ± 0.05	1.01	0.28

TABLE 4. Force coefficients obtained from experiments and corresponding numerical simulations. Displacements are given in primary body diameters. Coefficients are from the image data unless indicated otherwise.

and from the images (table 4). However, although we would expect the inclusion of the metal pipe necessary to protect the accelerometer cable to have a negligible effect on the measured forces in this zero-lift configuration, for those cases in which the secondary was exposed to the primary shock-processed flow, this would not necessarily be true. In particular, the lift could be affected by the presence of this tube in such configurations. Given the agreement that was observed between the two measurement methods in the validation experiment, as well as in two further experiments using identical configurations (T5 shots 2327 and 2328 – see table 4), it was decided to run the remaining proximal body experiments in the cleaner configuration obtained by removing the accelerometer and protective tube.

In those experiments in which the accelerometer was included, the model used was the Endevco model 7270-2K. The power spectrum of the acceleration signal obtained during T5 shot 2322 is shown in figure 14(*a*). The resonant frequency of this model is approximately 90 kHz, and a large peak in the spectrum is observed near this value, with another peak near 55 kHz. As our test time is of the order of 1 ms, it is a simple matter to remove these frequency components from the signal by the use of a low-pass filter. The signal resulting from this, and from further box-car smoothing, is shown in figure 14(*b*). As can be seen, the transient loading produced by the flow start-up is much larger than the loading produced during the steady-flow time.

6.4. *Numerical simulation of experiments*

For each of the experimental configurations, a perfect gas numerical simulation was carried out using the AMROC software. For the validation experiment, T5 shot 2322, the simulation was similar to those described earlier, albeit with a single sphere and appropriate values of M_∞ and γ (see below). A drag coefficient of 0.956 was calculated. For this configuration, simulations were also carried out by J. Olejniczak using the DPLR non-equilibrium code (see Wright, Candler & Bose 1998). This code includes viscous effects as well as source terms for chemical reactions and vibrational relaxation processes. The free-stream conditions were consistent with the experimental conditions at the relevant point downstream, and both reacting and perfect gas flows were simulated. A body-fitted grid with axisymmetric geometry was used. The drag coefficient in the perfect gas case was 0.997; that in the reacting case was 0.995. These differences are small and could be due to grid artefacts rather than reaction

https://doi.org/10.1017/S0022112007007987 Published online by Cambridge University Press

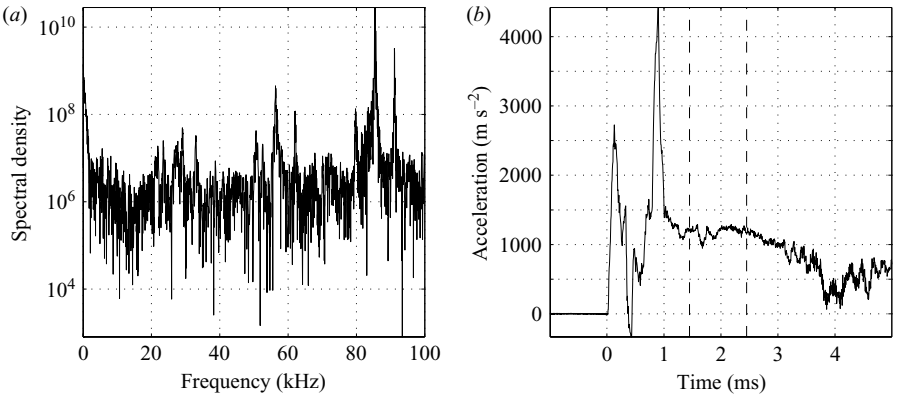


FIGURE 14. (*a*) Power spectrum of the accelerometer signal recorded during T5 shot 2322; (*b*) resulting signal after low-pass filtering and smoothing. The steady test time is indicated by the dashed vertical lines.

effects. We conclude that the effect of flow chemistry on the forces is small at these conditions, although viscous effects may contribute around 4 % to the drag.

For the remaining configurations, in order to simulate the flow produced by the conical nozzle of the T5, slightly divergent inlet flow was specified in a way consistent with the downstream location of the models. The ratio of specific heats was also consistent with the free-stream composition and temperature at the downstream location of the primary body. A value of $\gamma = 1.19$ was calculated using the NASA Glenn thermodynamics database tool, Thermobuild (see http://cea.grc.nasa.gov/).

The computational parameters for the numerical simulations were similar to those used in the three-dimensional refinement study described in § 4.3. Three additional levels of refinement were used over the base grid, with refinement factors of 3 at the highest level and 2 at lower levels. Referring to our error estimates from the refinement study then, we would expect refinement errors of, at most, 2 % and 5 % of the drag value, respectively, in the computational drag and lift coefficients. For the calculation of the computational force coefficients, the reference density and velocity were taken at the downstream location of the centre of the primary sphere, rather than at the inlet, to maintain consistency with the experimental coefficients.

6.5. *Results*

Figure 15 shows experimental and computational schlieren images from one experimental condition. As may be seen, the shock impingement points on the secondary body are relatively close, although the experimental shock radius appears slightly smaller. This may be partly due to the finite resolution of the simulation, given the effect of increases in resolution that has been noted in the refinement study. Also contributing to this discrepancy may be the lack of real-gas effects in the numerical simulation, as these are known to lead to a narrowing of the shock radius.

The force coefficients measured in the experiments are given in table 4 and compared with the corresponding computational coefficients. The axial and lateral relative displacements of the centres of the two bodies are given in terms of the primary body diameter. The shock position entry indicates the location of the primary bow shock relative to the secondary body. In most cases, the shock was impinging on the secondary body, a situation in which we have seen the lift value especially to be sensitive to the exact impingement point of the shock.

https://doi.org/10.1017/S0022112007007987 Published online by Cambridge University Press

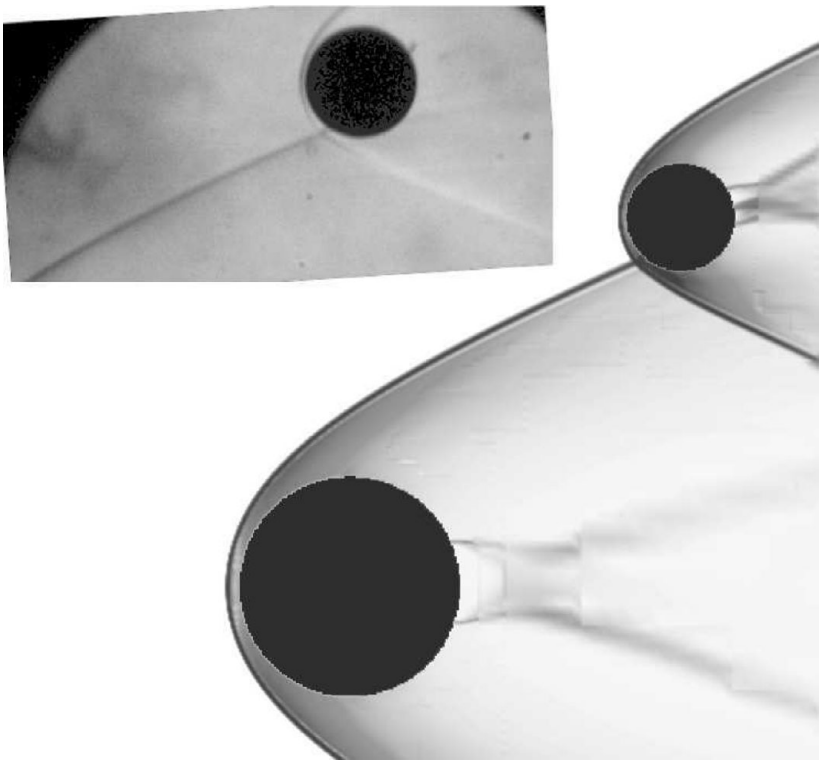


FIGURE 15. Experimental and computational schlieren images of T5 shot 2330. The experimental image has been rotated to correct for the rotation in the T5 optical system.

Overall, however, good agreement is obtained between the experimental and computational coefficients. The experimental drag values are consistently slightly higher than the computational values, but agree to within the measurement errors (agreement is obtained for shot 2330 if we include a refinement error of 2 %). The higher experimental values may be explained by the lack of viscous force components in the numerical simulations: we have noted that these can contribute around 4 % to the drag value, although this effect may be compensated for to some degree by the presence of the catcher in the experiments. The experimental lift values generally have relatively large errors associated with them owing to the small lift to drag ratios, but agreement is obtained to within the measurement error for three of the four cases, the exception being shot 2326.

7. Conclusions

The hypersonic proximal bodies problem has been explored for simple geometries using analytical modelling, numerical simulation and experiments.

An analytical methodology based on the blast-wave analogy was developed and used to model configurations consisting of two circular cylinders and two spheres. The forces acting on the secondary body were predicted for situations in which the secondary lies completely inside the primary bow shock. A strong body-size effect was observed in both cases that resulted in an increasingly negative lift coefficient as the secondary body size was increased. It was also found that, in the case of two spheres, a secondary body of diameter greater than approximately one-sixth that of

https://doi.org/10.1017/S0022112007007987 Published online by Cambridge University Press

the primary body would experience an exclusively negative lift coefficient inside the shocked region.

These configurations were also simulated numerically using the AMROC software and the resulting force coefficients were compared with those obtained from the analytical model. Reasonably good agreement was observed if the lateral displacement of the secondary was normalized by the shock radius in each case. The strong entropy wake in the blast-wave solution was noted to lead to discrepancies at smaller lateral displacements, however, especially in the spherical case.

Finally, a series of experiments was performed in the T5 hypervelocity shock tunnel. A new force-measurement technique was developed, and this was employed to measure the forces on the secondary body in several proximal spheres configurations. Perfect-gas numerical simulations of all run conditions were carried out, and generally good agreement was observed between the numerical and experimental force coefficients. The measurement technique provided two means of determining the drag force, and the agreement observed between these gives a further degree of confidence in the results obtained.

S. J. L. is grateful for assistance received from the Gordon and Betty Moore Fellowship and the Darryl G. Greenamyer Fellowship. R. D. was postdoctoral scholar in Applied and Computational Mathematics at the California Institute of Technology when this work was carried out. All authors gratefully acknowledge the provision of computational resources by the ASC Alliance Center for the Simulation of Dynamic Response of Materials which is supported by the ASC program of the Department of Energy under subcontract No. B341492 of DOE contract W-7405-ENG-48.

REFERENCES

Ambrosio, A. & Wortman, A. 1962 Stagnation point shock detachment distance for flow around spheres and cylinders. *ARS J.* **32**, 281.

Artem'eva, N. A. & Shuvalov, V. V. 1996 Interaction of shock waves during the passage of a disrupted meteoroid through the atmosphere. *Shock Waves* **5**, 359–367.

Artemieva, N. A. & Shuvalov, V. V. 2001 Motion of a fragmented meteoroid through the planetary atmosphere. *J. Geophys. Res.* **106** (E2), 3297–3309.

Berger, M. & Colella, P. 1988 Local adaptive mesh refinement for shock hydrodynamics. *J. Comput. Phys.* **82**, 64–84.

Billig, F. S. 1967 Shock-wave shapes around spherical- and cylindrical-nosed bodies. *J. Spacecraft Rockets* **4**, 822–823.

Carman, J. B., Jr 1980 Store separation testing techniques at the Arnold Engineering Development Center–Volume I: An Overview. *Tech. Rep.* AEDC-TR-79-1. Arnold Engineering Development Center.

Deiterding, R. 2003 Construction and application of an AMR algorithm for distributed memory computers. In *Adaptive Mesh Refinement–Theory and Applications.* Lecture Notes in Computational Science and Engineering vol. 1, pp. 361–372.

Deiterding, R. 2005 Detonation structure simulation with AMROC. In *High Performance Computing and Communications 2005*. Lecture Notes in Computer Science vol. 3726, pp. 916–927.

Deiterding, R., Radovitzky, R., Mauch, S. P., Noels, L., Cummings, J. C. & Meiron, D. I. 2005 A virtual test facility for the efficient simulation of solid materials under high energy shock-wave loading. *Engng Comput.* **22** (3–4), 325–347.

Hayes, D. H. & Probstein, R. R 1966 *Hypersonic Flow Theory*. Academic.

Hornung, H., Sturtevant, B., Bélanger, J., Sanderson, S. & Brouillette, M. 1991 Performance of the new free-piston shock tunnel T5 at GALCIT. In *Proc. 18th Int. Symp. on Shock Waves, Sendai, Japan.* Springer.

https://doi.org/10.1017/S0022112007007987 Published online by Cambridge University Press

Joarder, R. & Jagadeesh, J. 2004 A new free floating accelerometer balance system for force measurement in shock tunnels. *Shock Waves* **13**, 409–412.

Lees, L. 1955 Hypersonic flow. In *Proc. 5th Intl Conf. Los Angeles*, pp. 241–276. Inst. Aero. Soc., New York.

Lordi, J. A., Mates, R. E. & Moselle, J. R. 1966 Computer program for the numerical solution of nonequilibrium expansions of reacting gas mixtures. *NASA* CR-472.

Lukasiewicz, J. 1962 Blast-hypersonic flow analogy – theory and application. *ARS J.* **32**, 1341–1346.

McIntosh, M. K. 1969 A computer program for the numerical calculation of equilibrium and perfect gas conditions in shock tunnels. *Tech. Rep.* CPD 169. Australian Defense Scientific Service.

Mee, D. J. 2003 Dynamic calibration of force balances for impulse hypersonic facilities. *Shock Waves* **12**, 443–455.

Mee, D. J., Daniel, W. J. T. & Simmons, J. M. 1996 Three-component force balance for flows of millisecond duration. *AIAA J.* **34**(3), 590–595.

Meyer, S. L. 1975 *Data Analysis for Scientists and Engineers*. John Wiley.

Naumann, K. W., Ende, H., Mathieu, G. & George, A. 1993 Millisecond aerodynamic force measurement with side-jet model in the ISL shock tunnel. *AIAA J.* **31**(6), 590–595.

Passey, Q. R. & Melosh, H. J. 1980 Effects of atmospheric breakup on crater field formation. *Icarus* **42**, 211–233.

Robinson, M. J., Mee, D. J., Tsai, C. Y. & Bakos, R. J. 2004 Three-component force measurements on a large scramjet in a shock tunnel. *J. Spacecraft Rockets* **41**, 416–425.

Sahoo, N., Mahapatra, D. R., Jagadesh, G., Gopalakrishnan, S. & Reddy, K. P. G. 2003 An accelerometer balance system for measurement of aerodynamic force coefficients over blunt bodies in a hypersonic shock tunnel. *Meas. Sci. Technol.* **14**, 260–272.

Sanderson, S. R. & Simmons, J. M. 1991 Drag balance for hypervelocity impulse facilities. *AIAA J.* **12**, 2185–2191.

Schultz, P. H. & Sugita, S. 1994 Penetrating and escaping the atmospheres of Venus and Earth. In *Lunar and Planetary Science Conf. XXV*, pp. 1215–1216.

Sedov, L. I. 1959 *Similarity and Dimensional Methods in Mechanics*. Trans. ed. Maurice Holt. Trans. Morris Friedman from the 4th Russian edn. Academic.

Storkmann, V., Olivier, H. & Gronig, H. 1998 Force measurement in hypersonic impulse facilities. *AIAA J.* **36**, 342–348.

Tanno, H., Itoh, K., Saito, K., Abe, A. & Takayama, K. 2004 Shock wave interaction with a sphere in a shock tube. In *Intl Symp. on Interdisciplinary Shock Wave Research*, pp. 483–497. Interdisciplinary Shock Wave Research Center.

Taylor, G. I. 1950 The formation of a blast wave by a very intense explosion. *Proc. R. Soc. Lond.* A**201**, 159–174.

Toro, E. F. 1999 *Riemann Solvers and Numerical Methods for Fluid Dynamics*. Springer.

Warren, W. R, Kaegi, E. M. & Geiger, R. E. 1961 Shock tunnel experimental techniques for force and moment and surface flow direction measurements. *ARS J.* **31** (1), 82–83.

Woods, W. C., Holland, S. D. & DiFulvio, M. 2001 Hyper-X stage separation wind-tunnel test program. *J. Spacecraft Rockets* **38**, 811–819.

Wright, M. J., Candler, G. V. & Bose, D. 1998 Data-parallel line relaxation method for the Navier–Stokes equations. *AIAA J.* **36**, 1603–1609.

https://doi.org/10.1017/S0022112007007987 Published online by Cambridge University Press